Electron magnetic resonance as a tool to monitor charge separation and reactivity in photocatalytic materials

(Article begins on next page)

23 April 2024

Electron Magnetic Resonance as a tool to monitor charge separation and reactivity in photocatalytic materials.

Valeria Polliotto, Stefano Livraghi, Elio Giamello*.

Dipartimento di Chimica and NIS, Università di Torino, Via P. Giuria 7, 10125 Torino, ITALY

elio.giamello@unito.it

Keywords. EPR, photocatalytic oxides, charge carriers, electron trapping, hole trapping

Abstract

The present paper describes the role of Electron Paramagnetic Resonance in the investigation of fundamental phenomena occurring in heterogeneous photocatalysis namely the light-induced charge carrier separation, the stabilization of the carriers and their consequent surface reactivity. We will describe the behavior of a series of photoactive oxides (TiO_2, ZrO_2, $ZrTiO_4$ and ZnO) having different band gap showing the stabilization of the electrons and of the holes in all cases. The EPR technique discloses the nature of different stabilization sites (e.g. Ti^{4+}, Zr^{4+}, Zn^{2+}) for the electrons and monitors the hole trapping in terms of formation of $O^{\bullet-}$ centers. The electron transfer reactivity of the photogenerated carriers at the surface is then monitored using specific scavengers admitted in the gas phase over the solid, namely molecular oxygen and molecular hydrogen for electron scavenging and hole scavenging respectively. The method here illustrated is particularly useful to preliminarily check the features of newly prepared photocatalytic materials.

1. Introduction

Scientific research in the areas of photocatalysis and water photosplitting has been in continuous development over the past 30 years.[1-4] Photocatalytic and photoelectrochemical methods can be a response to the compelling environmental problems of our age. These problems are on one hand related to the accumulation of greenhouse gases in the atmosphere due to the vast use of fossil fuels and, on the other hand, those caused by the dispersion of pollutants in the atmosphere and in aquatic systems.

Heterogeneous photocatalysis techniques are based on the use of photoactive systems capable of collecting the energy of light and transforming it into chemical energy through redox processes. The most efficient of these systems are based on the use of solid semiconductors and, very often, oxides. Despite the success of some photocatalytic methods for the reduction of pollutants and of some devices for the production of hydrogen from water, almost all current systems do not yet satisfy the numerous conditions required to be used on large scale [5].

Metal oxides play a paramount role in the area of photocatalysis. This is due to the large number of compounds that can be prepared having a wide variety of electronic properties, to their relatively high stability and, in many cases, to the relatively low cost of the materials. For this reasons the research on oxide-based semiconductors, on their modifications and on the coupling of these systems with co-catalysts able to favor the surface reactivity is still living.

An ideal photocatalytic system for large scale applications should simultaneously have many properties that are often irreconcilable with each other. This solid (or a set of coupled solids) must have, first of all, the capability to harvest important fractions of the solar spectrum. Furthermore, favorable band potentials for the redox half-reactions are required together with a surface chemistry suitable for the redox process and/or the interaction with the co-catalysts.

The fundamental step of all photocatalysis process is the spatial charge separation induced by the irradiation of the solid with photons of suitable energy (equal of higher than the band gap energy value). This causes the

promotion of electrons (e^-) in the conduction band (CB) and the formation of holes (h^+) in the valence band (VB). In the case of a generic metal oxide this results in the process described by eq. 1[6]

$$MeO_x + h\nu \rightarrow e^-_{(CB)} + h^+_{(VB)} \qquad (1)$$
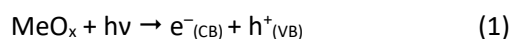
In order to understand the potentiality of an oxide in photocatalysis, it can be extremely useful to preliminarily evaluate its ability to undergo charge separation under illumination with different type of light (UV, Visible, etc) and, in parallel, its capability to transfer the charge carriers (electrons and holes) to molecules adsorbed on the surface. A preliminary evaluation of these properties can be used as a screening in particular when new types of potentially photocatalytic systems are identified and prepared. In our research group we have developed a systematic approach to study the charge separation and the ability of the photogenerated carriers to reach the surface based on Electron Paramagnetic Resonance (EPR) Spectroscopy. The EPR technique, in fact, is able to monitor paramagnetic centers. The stabilization of single charge carriers (either an electron or a hole) in an oxide (and in particular in diamagnetic oxides) indeed produces paramagnetic centers. Moreover, EPR, that make use of microwaves having frequencies of the order of the GHz for the spin excitation, can be used both in the dark and under illumination of light in the range of ultraviolet and visible frequencies providing a unique opportunity to study the excitation of photoactive systems under various types of irradiation.

The present paper is devoted to a short overview on the results obtained by this methodology during the investigation of various oxides interesting for photocatalysis. The nature of the trapped electron centers and of trapped hole ones will be firstly described. Secondly, the EPR tests to monitor the occurrence of a photoinduced charge transfer towards suitable electron or hole scavengers contacted with the surface of the solid will be illustrated.

EPR is a magnetic resonance technique based on the resonance of electron spin caused by microwaves when a sample containing paramagnetic centers is kept in a magnetic field. A classic (continuous wave) EPR spectrum reports a signal that is the first derivative of microwave absorption reported as a function of the magnetic field value. The theory of EPR is based on the spin-Hamiltonian formalism. The main terms of the latter are the

Zeeman interaction (electron spin-magnetic field interaction) ruled by the **g** tensor, determining the resonant field for a given species and the hyperfine interaction (electron spin – nuclear spin, **A** tensor) which describes the interaction of the unpaired electron with surrounding nuclei having non zero nuclear spin. The latter interaction, when present, allows mapping the spin density distribution in and around the paramagnetic centre. For a deeper introduction to the principles of the EPR technique and to its applications in solid state and surface chemistry the reader is referred to specific literature. [7,8]

2. Monitoring photoinduced charge separation and stabilization.

Irradiation of an oxide (equation 1), when performed under vacuum (i.e. in the absence of any possible surface reactivity), can lead to the stabilization of both excited electrons and holes at suitable sites of the solid. The recombination of excited carriers is of course an easy process (photocatalysis, after all, is based on the competition between charge separation and charge recombination) so that to observe the stabilization of the carriers, the experiment must be performed at low temperature
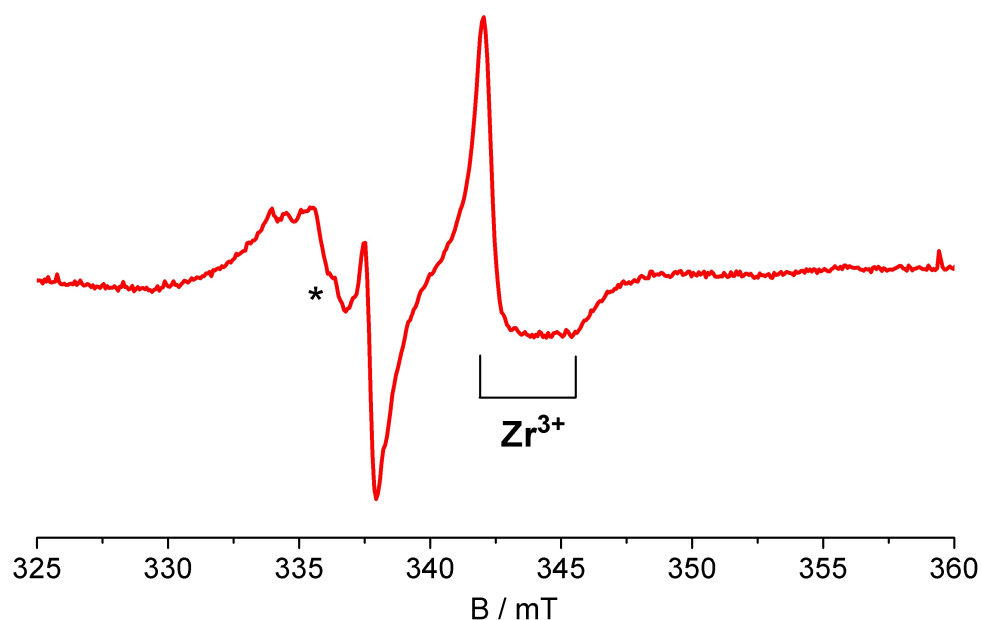

Figure 1. CW-EPR spectra of ZrO_2 recorded upon UV irradiation at 77 K under vacuum. The asterisk indicates the signal of the trapped hole (low field). The spectrum was recorded at microwave power of 10 mW.

. Fig. 1 shows the EPR spectrum obtained irradiating under vacuum at 77K with UV light a sample of zirconium dioxide.

The signals of the trapped hole (low field, l.h.s. of Fig. 1) and of the trapped electron (high field, r.h.s. of Fig. 1) fall in distinct regions of the whole EPR spectrum. This is the key factor allowing monitoring the charge carriers separation and stabilization. Rising the temperature to room temperature causes the recombination of almost all the carriers with vanishing of the EPR spectrum

.

*2.1 Monitoring photogenerated trapped electrons*

The stabilization of trapped electrons after photoexcitation depends on the nature of the oxide. Usually in a transition metal oxide the electrons tend to be stabilized on the metal ions according to:

$$Me^{n+} + e^- \rightarrow Me^{n-1} \qquad (2)$$
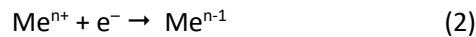
An alternative is the stabilization of the photogenerated electron into an oxygen vacancy. This occurs, however, particularly in the case of non-transition metal oxides such as alkali earth oxides.[9] In this case both bulk oxygen vacancies (Schottky defects) and surface cationic sites can act as electron traps [10]. In both cases the stabilization of the electrons generates paramagnetic species, therefore EPR spectroscopy is the most suitable technique to study the trapped charge and to provide information about the symmetry and the spin distribution of the paramagnetic center.

In the following, some examples of photogenerated electron stabilization on widely known metal oxides will be provided.

In titanium oxide electrons formed by photoexcitation are trapped by Ti^{4+} ions forming Ti^{3+} ions as shown by a series of EPR results (eq. 3)[11-15]

$$Ti^{4+} + e^-_{(CB)} \rightarrow Ti^{3+} \qquad (3)$$
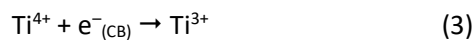
The stabilization of photoexcited electrons in oxygen vacancies of TiO_2 has been invoked in more than one case [16]. However, in our opinion, a true, unambiguous evidence of such centers (F-centers in terms of defect chemistry) has never been provided and accurate theoretical calculation clearly point to the stabilization of electrons in Ti d orbitals even in the presence of a nearby oxygen vacancy. [17]

The EPR spectra of electrons trapped by three different titania polymorph obtained irradiating the sample with UV light are reported in Figure 1 and the related g values are reported in Table 1. Ti^{3+} is a paramagnetic (S=1/2) ion with $3d^1$ configuration. In the solid matrix the ground state of the free ion is split by the effect of a crystal field that, in the three main TiO_2 polymorphs, has octahedral symmetry. In this case the free-ion ground state is split to give two subgroups with three t_{2g} and two e_g orbitals separated by the energy term Δ_O. An additional tetragonal or trigonal distortion further lifts the degeneracy of the t_{2g} and e_g levels and results in an anisotropic g tensor. The principal values of this tensor mainly depend on the energy splitting between the various d-orbitals as determined by the crystal fields and the various distortions. For a more detailed treatment of this subject the reader is referred to previous papers. [15,17]

In anatase (Figure 2a) two main paramagnetic species amenable to Ti^{3+} ions are identified, the former is an axial signal (signal I) with $g_{//}$ = 1.992 and $g_{\perp}$ = 1.962 and has been assigned to reduced Ti^{3+} centers in regular lattice sites of the anatase matrix. The second is a broad line (signal II) centered at g = 1.93 and is assigned to a collection of slightly different Ti^{3+} centers located at the surface, or in the subsurface region.[18] This assignment is supported by clear experimental evidence obtained using ^{17}O enriched TiO_2 and monitoring the electron spin density around the Ti^{3+} center. The broad line typical of signal II is in agreement with the assignment to surface centers since the linewidth witnesses the presence of a disordered environment such that available at the surface of nanostructured materials.

In rutile (Figure 1b) two are the main Ti^{3+} paramagnetic species that arise after UV irradiation in vacuum. The first is a rhombic signal with g_1 = 1.970, g_2 = 1.961 and g_3 = 1.948 (signal III) identified with Ti^{3+} centers at the surface or near the surface of crystals. The second one is a signal with rhombic symmetry with g_1 = 1.966, g_2 =

1.961 and $g_3 = 1.948$ (signal IV) that is assigned to Ti^{3+} centers at the regular (i.e. non interstitial) cationic sites of the bulk rutile structure.[19]

In the case of brookite (Figure 1c) the signal resulting from Ti^{3+} ions in bulk lattice site is a signal with axial symmetry and g values $g_{//} = 1.989$ and $g_{\perp} = 1.960$ (signal V). A broad signal centered at $g = 1.93$ (signal VI) is again assigned to surface Ti^{3+} sites (heterogeneity of sites).[19]

I (Anatase)		$g_{//} = 1.992$	$g_{\perp} = 1.962$
II (Anatase)		$g_{average} = 1.93$	
III (Rutile)	$g_1 = 1.970\ (1.973)$	$g_2 = 1.961$	$g_3 = 1.948$
IV (Rutile)	$g_1 = 1.966$	$g_2 = 1.961$	$g_3 = 1.948$
V (Brookite)		$g_{//} = 1.989$	$g_{\perp} = 1.960$
VI (Brookite)		$g_{avarage} = 1.93$	

Table 1. g values of Ti^{3+} signal on the different TiO_2 polymorph deriving from the EPR signals of Figure 1.

Interestingly the three EPR lines have a different profile in the three cases. The spectra of anatase and brookite actually are quite similar but not identical, while that of rutile is markedly different from the others. Considering that in all three cases we have titanium ions surrounded by oxygen ions in octahedral coordination, the distinct profiles reported in Fig. 2 indicates a strong sensitivity of the technique to the structural parameters (crystal field strength and related distortions).

In photocatalytic reactions performed using titanium dioxide, the maximum photocatalytic activity is nearly always observed in the case of the commercial P25, a material produced by Degussa that has become a sort of benchmark in the world of applied photocatalysis. This solid is prepared by flame spray synthesis and it is made up of rutile and anatase phases partially connected by a specific interface.[20] To confirm the effectiveness of the EPR analysis here described, the signal of P25 upon UV irradiation (Figure 3c) is clearly interpreted in terms of the overlap of the signals of Ti^{3+} of both anatase (Figure 3a) (signals I and II) and rutile (Figure 3b) (signals III and IV).
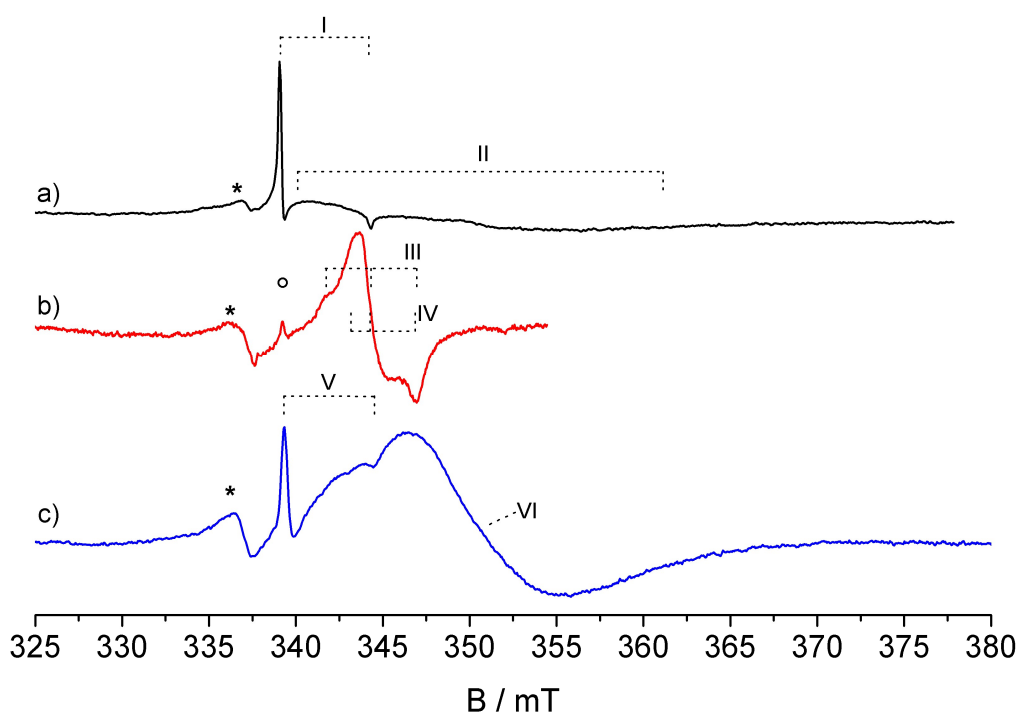
Figure 2. Normalized CW-EPR spectra of a) anatase, b) rutile and c) brookite polymorph recorded upon UV irradiation at 77 K in vacuum. The asterisks indicate the signals of the trapped holes and the circle indicates traces of Ti^{3+} in the anatase impurity. Spectra were recorded at microwave power of 10 mW.
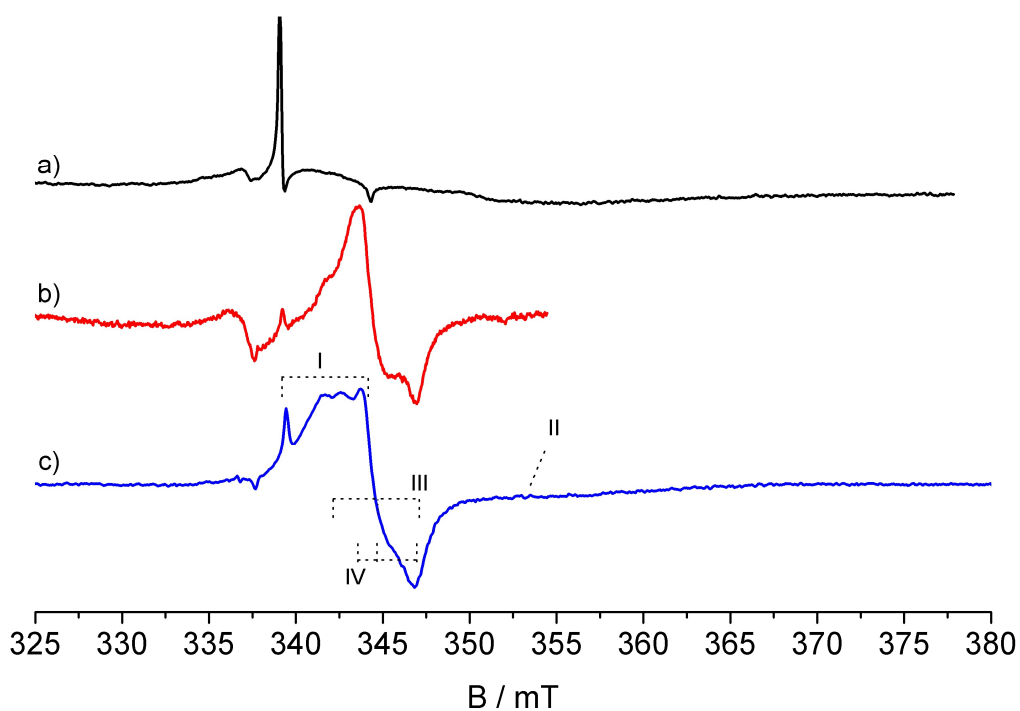

Fig. 3 Normalized CW-EPR spectra of a) anatase, b) rutile and c) P25 recorded upon UV irradiation at 77 K in vacuum. Spectra were recorded at microwave power of 10 mW.

To conclude, the above experiments show that in TiO_2 the electrons generated upon irradiation at low temperature migrate into the solid and are distributed between surface and bulk Ti trapping sites.

Zirconium dioxide (zirconia) is an oxide with large band gap energy (ca. 5.5 eV) requiring high energy UV photons for excitation. For this reason, bare ZrO_2 has been hardly used in photocatalysis [21]. However, quite recently, systems based on zirconia doped with cerium ions have been reported as they show interesting photoactivity properties under visible light that are related to the presence of cerium. [22,23]. In the case of the pristine zirconium dioxide matrix the electrons generated by irradiation are stabilized on Zr^{4+} ions forming Zr^{3+} ions as shown in Fig. 1 in the case of a solid prepared via sol-gel. The signal belonging to Zr^{3+} ions has spectral features similar to those of Ti^{3+} due to the analogy of electronic configuration ($4s^1$ in this case). In particular it corresponds to an axial trace with $g_{//}$ = 1.9768 and $g_{\perp}$ = 1.9589 assigned to Zr^{3+} bulk species.[24] The important fraction of electrons trapped at the surface, detected in the case of titanium dioxide, is , in the case of zirconia, less evident.

Zirconium titanate ($ZrTiO_4$) represents an interesting model to study the effect of modulation of the band gap value and of the band potentials being midway, in term of composition, between titania and zirconia maintaining structural features similar to those of TiO_2 (scrutynite structure based on connections of TiO_6 octahedra). The EPR spectrum of zirconium titanate ($ZrTiO_4$) upon UV irradiation in vacuum at 77 K is reported in Figure 4. Irradiation of this oxide containing both Ti and Zr ions in equivalent amount, causes the formation of both Zr^{3+} and Ti^{3+} signals. The Zr^{3+} signal have $g_{//}$ = 1.978 and $g_{\perp}$ =1.960, analogously to what occurs in pure ZrO_2. The Ti^{3+} signal is broad and centered at g =1.93 amenable to surface species. The amount of Ti^{3+} ions looks higher than that of Zr^{3+} ones since the empty 3d states of titanium ions are lower in energy than those of zirconium ones (4d) thus inducing the preferential stabilization of photoexcited electrons.[25]
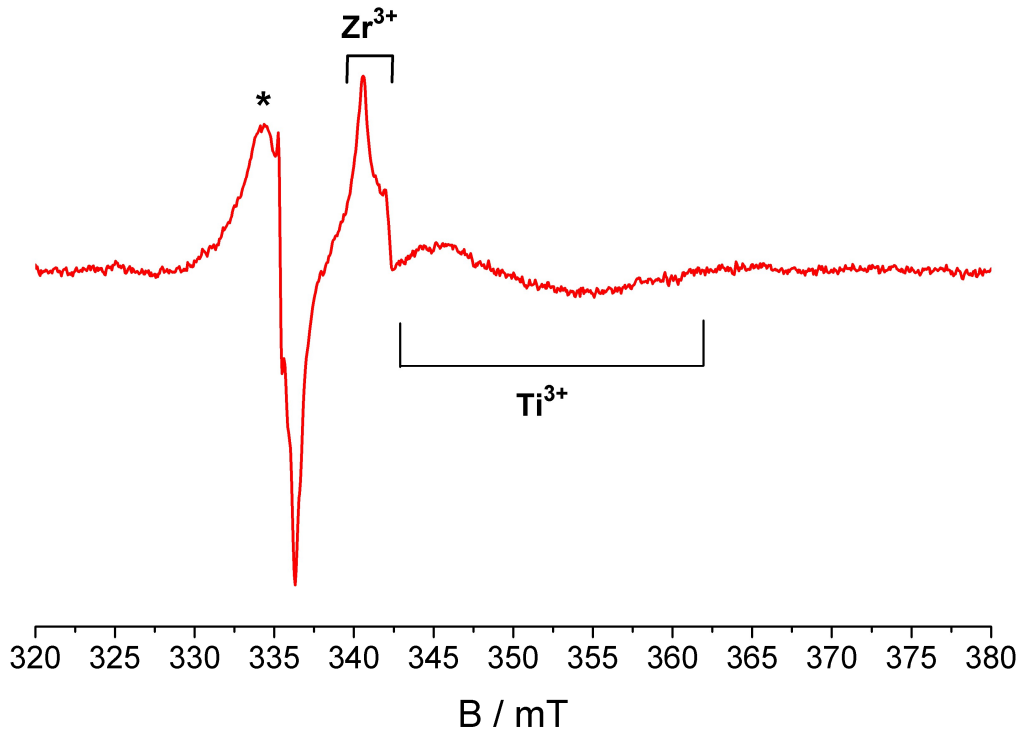
Figure 1. CW-EPR spectra of ZrTiO$_4$ recorded upon UV irradiation at 77 K in vacuum. The asterisk indicates the signal of trapped holes. The spectrum was recorded at microwave power of 10 mW.

Electron trapping upon irradiation of ZnO causes the growth of a symmetric signal centered at g= 1.96. The nature of this signal has been already discussed in the past and the most reliable interpretation is in terms of the formation of Zn$^+$ (eq. 4).[26,27]

$$Zn^{2+} + e^-_{(CB)} \rightarrow Zn^+ \qquad (4)$$

Even though some Author assigns the symmetric signal to an F center (an electron trapped in an oxygen vacancy) the assignment to interstitial Zn$^+$ ions [28] seems the most reasonable one also on the basis of the propensity of reducible oxides to stabilize electrons on cations. The interstitial nature of this center is explained in terms of the size of the monovalent cation which is bigger than Zn^{2+} and therefore it is more easily accommodated in the octahedral cavity available in the wurtzitic structure of the solid rather than in the smaller regular tetrahedral site.
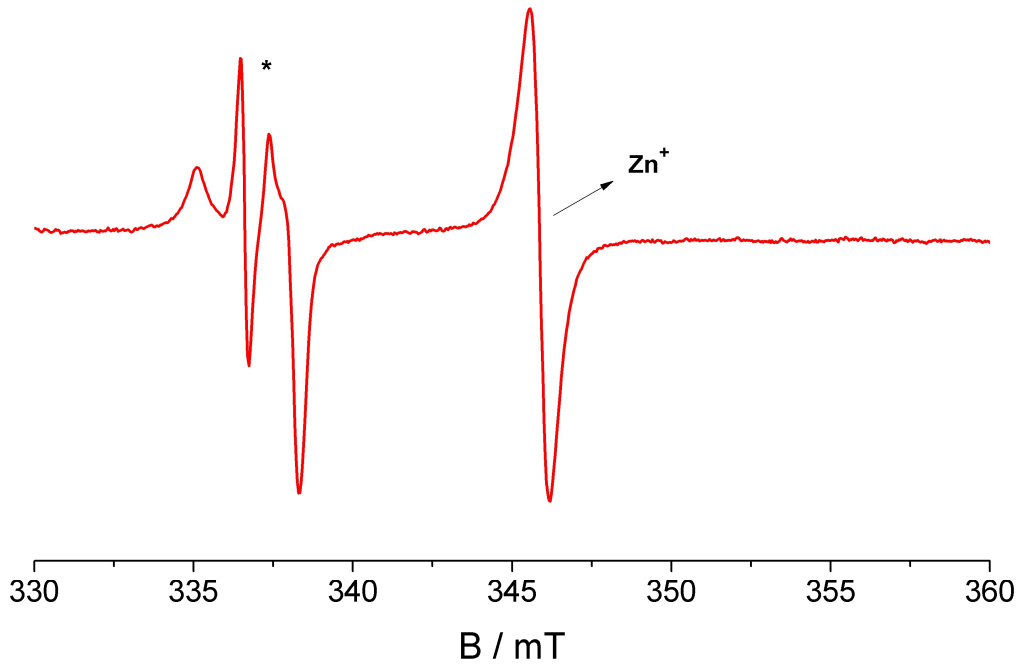
Figure 2. CW-EPR spectra of ZrTiO₄ recorded upon UV irradiation at 77 K in vacuum. The asterisks indicate the signal of the trapped holes. Spectrum was performed at microwave power of 10 mW.

2.2 Monitoring photogenerated trapped holes.

The sites responsible for the stabilization of the holes in metal oxide are the oxygen ions of the lattice (O^{2-}) that

form paramagnetic $O^{\bullet-}$ species (eq. 5)

$$O^{2-} + h^+_{(VB)} \rightarrow O^{\bullet-} \tag{5}$$

This ion bears an unpaired electron and can be observed, in many cases, using EPR. The observation of the EPR

signal of an $O^{\bullet-}$ centre is therefore diagnostic of hole trapping into the system.

The expected structure of the **g** tensor for the $O^{\bullet-}$ radical ion (electron configuration $2p_x^2$, $2p_y^2$, $2p_z^1$) has been

discussed years ago by Brailsford.[29] In the most general case of rhombic symmetry, and neglecting second-

order terms, one has (eq. 6)

$$g_{zz} \approx g_e \qquad g_{xx} = g_e + \frac{2\lambda}{\Delta E_1} \qquad g_{yy} = g_e + \frac{2\lambda}{\Delta E_2} \tag{6}$$
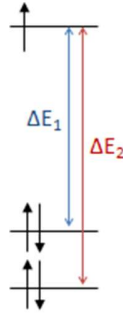
11

Figure 3. Crystal field effects on a O$^-$ radical ion.

where g_e is the free spin value (2.0023), λ is the spin-orbit coupling constant, which for atomic oxygen is 135 cm^{-1}, and ΔE_1 and ΔE_2 are the energy differences corresponding to the separation between the 2p$_z$ and the other two p-orbitals induced by crystal field effects, as shown in Figure 6.[30] The signal of the O$^{\bullet-}$ species therefore is characterized by g>2.00 and lies at fields well separated from those of the trapped electron resonance that are, as before illustrated, at g<2.00.

A specific study about the nature of holes was performed in anatase and two families of O$^{\bullet-}$ species photogenerated by UV irradiation have been observed (Figure 7a and b, Table 2).[31] Species 2, with g value g_1 = 2.016, g_2 = 2.011 and g_3 = 2.005 is present on both hydrated and dehydrated surfaces and is O$_2$ insensitive (Fig. 7b). This means that its signal is not perturbed by the physisorption of an O$_2$ layer at the surface. Since the O$_2$ molecule is paramagnetic (S=1), a second paramagnetic species, if located at the surface, undergoes dipolar interaction with O$_2$ with consequent broadening of its EPR signal. Since broadening is not observed in this case, the signal has been assigned to a O$^{\bullet-}$ species located under the surface as a three-coordinated (bulk) center. The O$^{\bullet-}$ species labelled with 1 is characterized by a more anisotropic **g** tensor (g_1 = 2.029, g_2 = 2.017 and g_3 = 2.004) and is observed on hydrated surfaces only and its EPR signal practically vanishes upon O$_2$ physisorption (compare Fig. 7a and 7b). Species 1 is, thus, more exposed at the surface of the oxide than species 2 and has

been assigned to an hole stabilized by a surface two-coordinated oxygen.[31] Remarkably the same signal observed after oxygen physisorption (Fig. 7b) is also recorded upon irradiation of sample carefully dehydrated at high temperature. This confirm the previous assignment about the role played by surface water in the stabilization of the photogenerated holes.[31] The presence of molecular water and of surface hydroxyls groups in fact favors the stabilization of trapped holes on the anatase surface (species 2). The most abundant production of hole centers is, in fact, observed when both surface hydroxyl groups and physisorbed water are present on the anatase surface (spectrum 7a). This feature is relevant for the mechanisms of photocatalytic reactions performed in water suspensions that are the large majority.
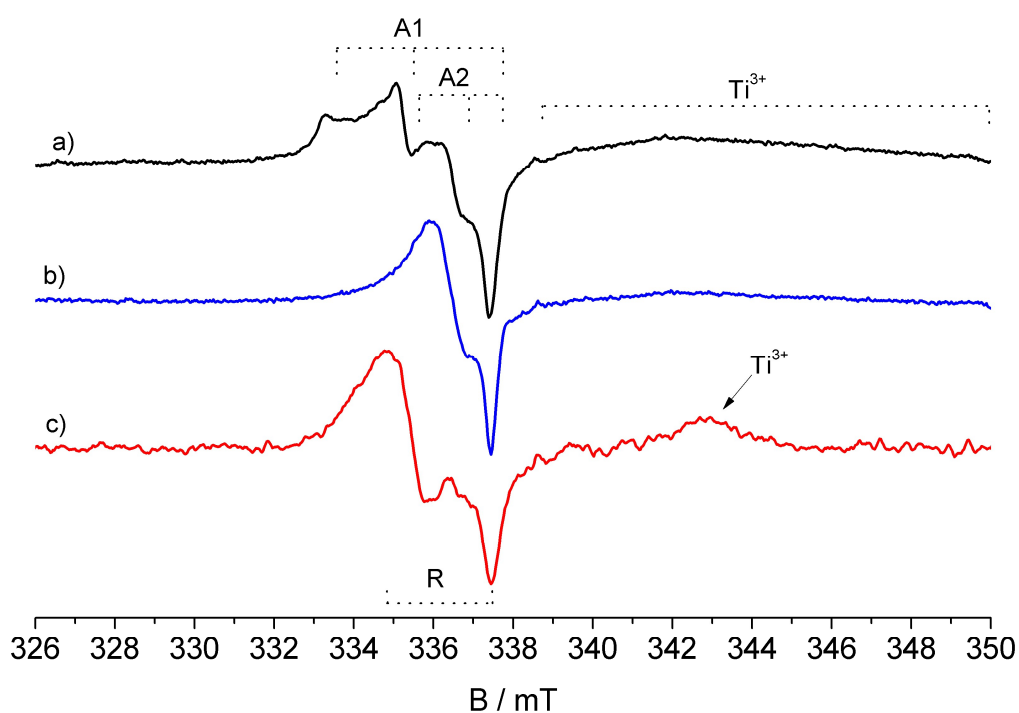

Figure 4. Normalized CW-EPR spectra of hole centers in UV irradiated TiO_2 systems. Spectrum a) is obtained with an as prepared (surface hydrated) anatase (species 1 and 2). Spectrum b) is observed after physisorption of molecular oxygen on the same sample (a) and also in the case of fully dehydrated anatase (species 2 only). Spectrum c) corresponds to an as prepared rutile. All the spectra are recorded after UV-irradiation under vacuum at 77 K at microwave power of 1 mW.

A preliminary study on photogenerated hole has been performed also on rutile and the EPR spectrum is reported in Figure 7c. Since an accurate study, as in the case of anatase, on this polymorph was not performed,

the presence of more $O^{\bullet-}$ species cannot be excluded but the observed g values (g_1 = 2.019, g_2= 2.004, Table 2) are in good agreement with the results concerning holes trapped at the lattice oxygen atoms found by Kumar et al. located in the subsurface layer with g values g_1 = 2.019, g_2 = 2.014 and g_3 = 2.002.[32]

Table 2 resumes the g factors of hole centers monitored by EPR in anatase and rutile.

	g_1	g_2	g_3
ANATASE species 1	2.016	2.011	2.005
ANATASE species 2	2.029	2.017	2.004
RUTILE		2.019	2.004

Table 2. g tensors of hole centers monitored by EPR in the two main polymorphs of titanium dioxide.

Figure 8 show the hole ($O^{\bullet-}$) species generated by the UV irradiation in vacuum of ZrO_2 (Figure 8a), $ZrTiO_4$ (8b). and ZnO (8c) . In the first and second case the hole signals are characterized by a rhombic g tensor with g values g_1 = 2.022, g_2 = 2.015, and g_3 = 2.004 for ZrO_2,[24,31,33] while g_1 = 2.014, g_2 = 2.010, and g_3 = 2.005 in the case of $ZrTiO_4$.[25] In parallel electron trapping sites (Ti^{3+} and Zr^{3+}) are photoformed (see Section 2.1).

It is worth to note that the EPR spectra of hole centers in these MeO_2 have a rhombic **g** tensor ($g_{xx} \neq g_{yy} \neq g_{zz}$). In the structure of TiO_2 and $ZrTiO_4$, the O^{2-} ions are tricoordinated, while, in the monoclinic structures of zirconia, both tricoordinated and tetracoordinated sites are present. However, as it has been shown, the EPR features are very similar in all the systems because the holes tend to localize on tricoordinated sites also in the case of the monoclinic solid. Moreover, the first information derived from the **g** tensor is that the trigonal environment around the $O^{\bullet-}$ ion is distorted in all solids, since, for a true trigonal coordination, an axial structure of the tensor should be found ($g_{zz} = g_{yy} \neq g_{xx}$).

In the case of ZnO the EPR signal of a photogenerated hole is quite different and is reported in Figure 8c. In this case two different photogenerated holes centers are observed both with an axial **g** tensor indicating a more symmetric geometry of $O^{\bullet-}$ with respect to the previously described oxides. The first photogenerated hole

species (signal I of Figure 8c) is characterized by g values $g_\perp$ = 2.023 and $g_{//}$ = 2.003 while the second (signal II of Figure 8c) is characterized by $g_\perp$ = 2.008 and $g_{//}$ = 2.003.[34,35]
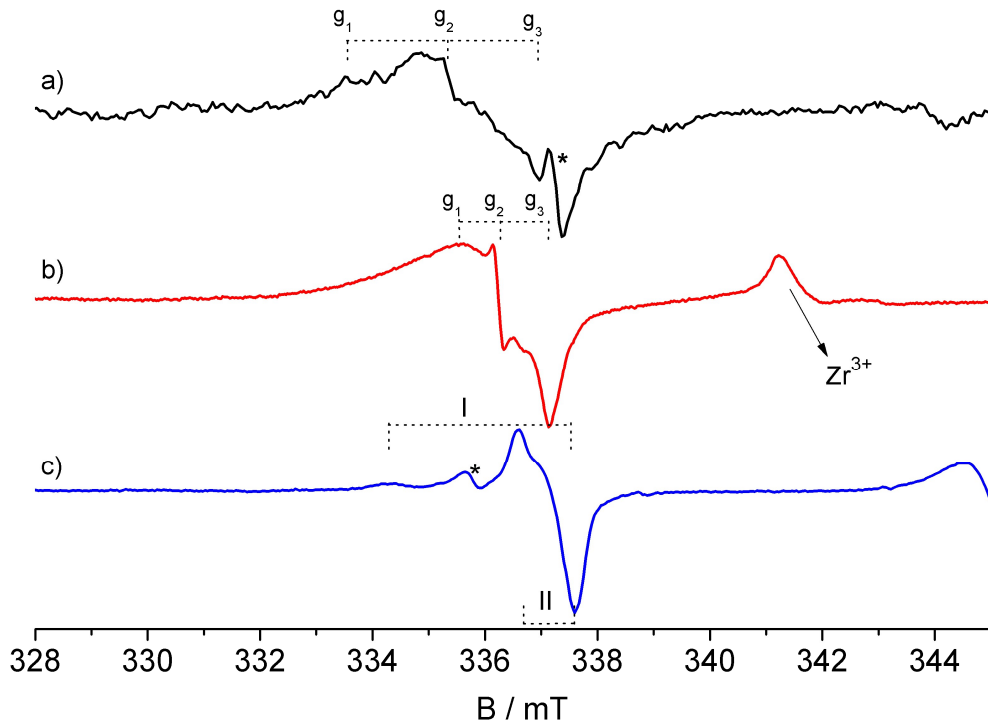

Figure 5. Normalized CW-EPR spectra of hole centers in a) ZrO_2, b) $ZrTiO_4$ and c) ZnO formed upon UV-irradiation under vacuum at 77 K. Asterisks indicate spurious EPR signals. Spectrum was performed at microwave power of 1 mW.

3. Holes in Al-doped MeO_2 oxides.

Information derived from the EPR spectra for the hole centers in bare MeO_2 oxides are limited to the **g** tensor since ^{16}O does not generate a hyperfine structure (^{16}O nuclear spin I = 0) and therefore does not provide any information about the spin density distribution over the oxygen hole center. For this reason doping of the matrix with ^{27}Al ions having nuclear spin I = 5/2 has been revealed interesting.[36]

The EPR spectra of photogenerated hole of Al-TiO_2 (spectrum a) and Al-ZrO_2 (spectrum b) are reported in Figure 9 and the spin Hamiltonian parameters are reported in Table 3. The difference from the g values of the

15

doped oxides with respect to the pristine materials (see Figure 7 and 8) is due to the distortion of the structure caused by the introduction of the dopant resulting in a higher degree of g rhombicity.
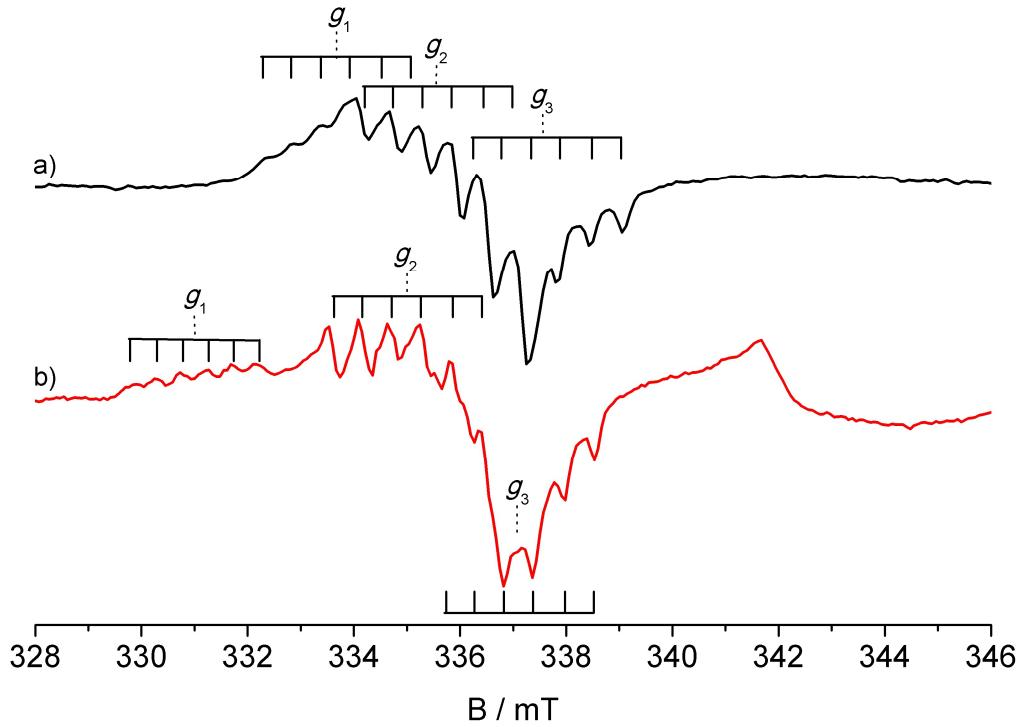

Figure 6. CW-EPR spectra of bulk hole centers in (a) Al-doped TiO_2 and (b) Al-doped ZrO_2. The spin Hamiltonian are listed in Table 3.

	g_1	g_2	g_3	A1	A2	A3
Al-TiO_2	2.026	2.014	2.003	- 0.529	- 0.603	- 0.606
Al-ZrO_2	2.041	2.017	2.004	- 0.490	- 0.560	- 0.567

Table 3. Spin Hamiltonian parameters of the spectra of Figure 9.

The EPR spectra of both doped oxides are characterized by rhombic symmetry and by a superhyperfine structure due to the interaction of the unpaired electron with a single neighboring Al dopant ion. Indeed, the three components of the rhombic **g** tensor of the $O^{\bullet-}$ species are nicely split in six hyperfine lines (2I + 1, I=5/2). This result indicates that the holes preferentially localize on oxygen ions having one dopant Al ion as neighbors. This occurs because the lattice distortion, induced by the presence of the aliovalent ion, stabilizes this particular hole-site with respect to the regular ones. In other words, the distortion induced by the dopant ion stabilizes the hole trapping center.

Finally, the study of the hyperfine constant reveals that the resolved superhyperfine structure of the spectra actually corresponds to a very weak delocalization of the spin density toward the Al dopant orbitals in both cases. This confirm the theoretical forecast describing the hole centers in oxide system as containing an unpaired electron tightly localized in a p orbital of the oxygen anion.

4. Charge carrier's reactivity

In order to evaluate the capability of the charge carriers photogenerated in an oxide matrix of reaching the surface of the nanoparticles and of reacting with adsorbed molecules, the EPR spectra under irradiation can be performed in presence of selective scavengers admitted in the gas phase. We adopt as gaseous scavengers O_2 and H_2 for photogenerated electrons and holes respectively.

The gas phase O_2 molecules in contact with the solid can react with photogenerated electrons, capable of reaching the surface, producing superoxide $O_2^{\bullet-}$ (usually adsorbed on a surface cation) following equation 7.

$$O_{2\,(gas)} + e^-_{(CB)} \rightarrow O_2^{\bullet-}_{(ads)} \qquad (7)$$
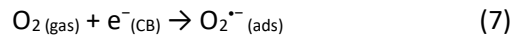
The detection by EPR of $O_2^{\bullet-}$ upon irradiation under O_2 is, thus, the evidence of the generation of surface reacting electrons. The superoxide radical ion is paramagnetic as it contains an unpaired electron in a 2p* antibonding orbitals. The EPR features of this species are based on the g tensor whose components are:

$$g_{xx} = g_e; \quad g_{yy} = g_e + 2\lambda/E; \quad g_{zz} = g_e + 2\lambda/\Delta \qquad (8)$$

where g_e and λ have the usual meaning (see before), Δ is the separation between the two π^* orbitals of the adsorbed superoxide caused by the electric field of the adsorption site and E is the separation between the highest of the two p orbitals and the 2s orbital. Being Δ much smaller than E, g_{zz} is the tensor component more differing from g_e and characterizes the adsorbed species being connected to the charge/volume ratio of the adsorption site. The g_{zz} parameter is therefore diagnostic of the surface site adsorbing the superoxide ions.[37]

As an example, the EPR spectrum of $ZrTiO_4$ oxide irradiated under oxygen atmosphere is reported in Figure 10 and is characterized by a typical spectrum of the superoxide $O_2^{\bullet-}$ ions characterized by a rhombic **g** tensor (eq.8). The signal is characterized by a g_{zz} region (lower magnetic field) with two resolved components indicating the presence of $O_2^{\bullet-}$ adsorbed on both titanium and zirconium tetravalent surface ions (*g* values in Table 4). The first g_{zz} component (*g* = 2.030) corresponds to superoxide ions adsorbed on Zr^{4+} ions, while the second one (*g* = 2.022) is due to $O_2^{\bullet-}$ on Ti^{4+} ions.[25,38] This indicates that both zirconium and titanium ions are exposed at the surface of the material and allow the reactivity between the photogenerated electrons and the oxygen molecules.
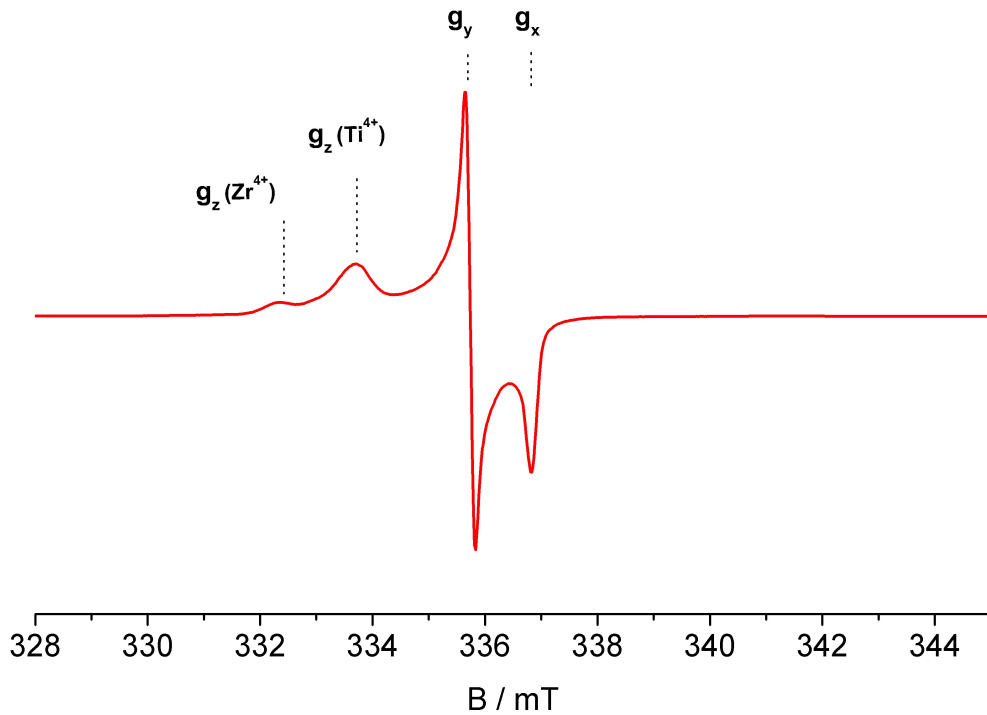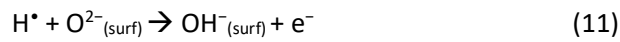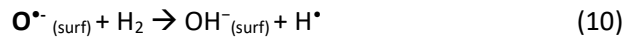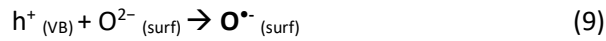

Figure 10. EPR spectra of a $ZrTiO_4$ sample irradiated in O_2 atmosphere with UV light at 77K. The spectrum was recorded at 77K and with a microwave power of 1 mW.

g_{zz}	g_{yy}	g_{xx}	description
2.022	2.010	2.003	$O_2^{\bullet-}$ on Ti^{4+}
2.030	2.010	2.003	$O_2^{\bullet-}$ on Zr^{4+}

Table 4. *g* value of superoxide species adsorbed on a $ZrTiO_4$ material.

The holes transfer capability can be tested irradiating the oxides under H_2 atmosphere. Under such conditions, those holes photogenerated in the valence band and capable to reach the surface interact with molecular hydrogen (H_2) with a peculiar reactivity based on H abstraction from H_2 and generation of reactive hydrogen atoms (eq. 10). $H^\bullet$ atoms, in turn, react at the surface, injecting electrons into the solid (eq. 11)[39] which follow the same channel of stabilization before illustrated for photogenerated electrons (stabilization on an electron trapping site). The final evidence of surface hole reactivity is thus the formation of reduced, EPR visible, species (Ti^{3+}, Zr^{3+}, …) due to the electron generated according to equation 11.

$$h^+_{(VB)} + O^{2-}_{(surf)} \rightarrow \mathbf{O^{\bullet -}}_{(surf)} \quad\quad (9)$$

$$\mathbf{O^{\bullet -}}_{(surf)} + H_2 \rightarrow OH^-_{(surf)} + H^\bullet \quad\quad (10)$$

$$H^\bullet + O^{2-}_{(surf)} \rightarrow OH^-_{(surf)} + e^- \quad\quad (11)$$

The effect on the EPR spectra of the irradiation in H_2 atmosphere of $ZrTiO_4$ is reported in Figure 11. Upon UV irradiation very intense signals typical of Zr^{3+} and Ti^{3+} arise.

The formation of these reduced species is due to a double effect. We have in fact both direct trapping the photogenerated electrons (Section 2.1) and trapping of electrons deriving from the reaction of holes with H_2 molecules (eq. 9 – 11).[39]

Differently from the case of irradiation under vacuum that generates an equivalent amount of electrons and holes which rapidly recombine upon rising the temperature (see comment to Fig. 1), in the present case there is no recombination upon rising T since the photogenerated holes have been consumed by the reaction illustrated above that produces a further amount of electrons.
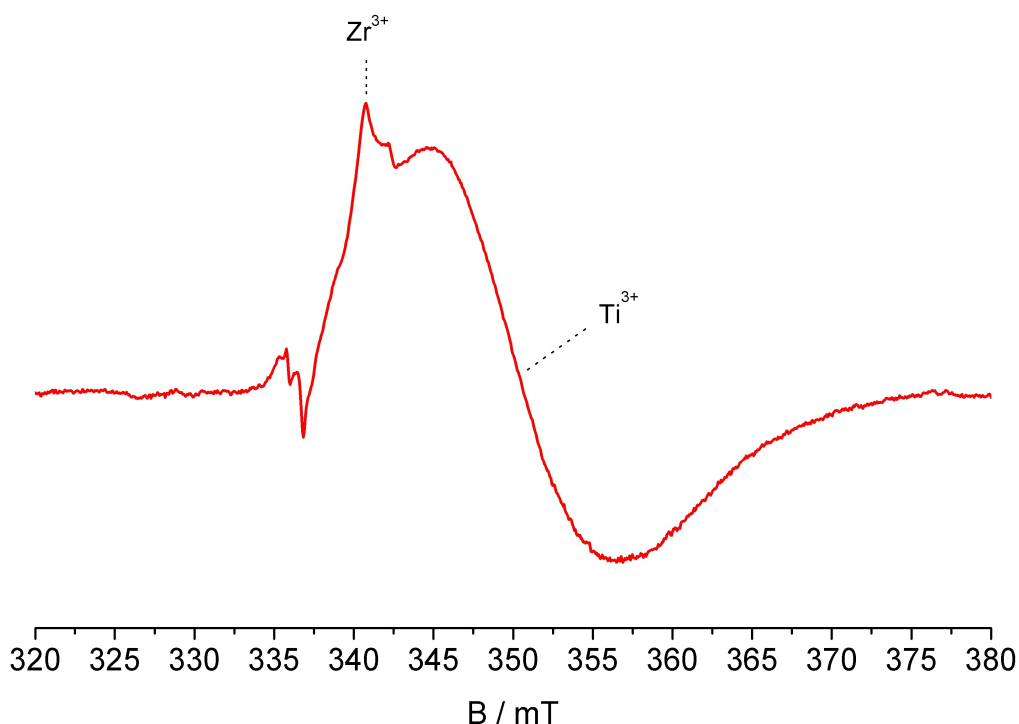
Figure 7. EPR spectra of $ZrTiO_4$ sample irradiated in H_2 atmosphere with UV light at 77 K. The spectrum was recorded at 77 K and with a microwave power of 10 mW.

5. Conclusions

In the present work we have pointed out the importance of EPR spectroscopy in the investigation of charge carriers separation and stabilization in semiconducting oxides under direct irradiation. Following, as an example, the behavior of a series of photoactive oxides (TiO_2, ZrO_2, $ZrTiO_4$ and ZnO) having different band gap, we have described the process leading to the stabilization of photogenerated charge carriers. We have also described the EPR features of trapped-electron and trapped-hole centers in all cases, outlining that the presence of reducible cations directs the stabilization of the excess electron towards the cation itself rather than towards oxygen vacancies. The EPR technique is useful in this case to distinguish different stabilization sites (e.g. Ti^{4+}, Zr^{4+}, Zn^{2+}) for the electrons. The holes are instead stabilized onto oxygen anions so that the EPR spectra of trapped holes ($O^{\bullet-}$ center) monitor the occurrence of hole trapping. Finally, the reactivity of the photogenerated carriers at the surface is monitored using specific scavengers admitted in the gas phase over the solid. These entails specific reactions ending up with the formation of paramagnetic centers witnessing the occurrence of surface electron transfer processes.

References

1 K. Hashimoto, H. Irie, A. Fujishima, Jpn. J. Appl. Phys. **44** 8269 (2005).

2 J. Schneider et al. Chem. Rev. **114**, 9919 (2014),

3 T. Hisatomi, J. Kubota, K. Domen, Chem Soc. Rev. **43**, 7520 (2014),

4 Y. Tachibana, L. Vayssieres, J. R. Durrant, Nature Photonics **6**, 511 (2012)

5 J. R. McKone, N. L. Lewis, H. B. Gray, Chem. Mat. **26**, 407 (2014)

6 A. L. Linsebigler, G.Q. Lu and J. T. Yates, Chem. Rev. **95**, 735 (1995)

7 M. Chiesa, E. Giamello, M. Che, Chem. Rev. **110**, 1320 (2010)

8 M. Brustolon, E. Giamello eds. EPR A practitioner toolkit, Hoboken, NJ (2009).

9 M. Chiesa, M.C. Paganini, G. Spoto, E. Giamello, C. Di Valentin, A. Del Vitto, G. Pacchioni, J. Phys. Chem. B **109**, 7314 (2005)

10 M. Chiesa, M.C. Paganini, E. Giamello, D.M. Murphy, C. Di Valentin, G. Pacchioni, Acc. Chem. Res. **39**, 861 (2010)

11 R.F. Howe M. Graetzel J. Phys. Chem. **89**, 4495 (1985)

12 O.I. Micic, Y.N. Zhang, K.R. Cromack, A.D. Trifunac and M.C. Thurnauer, J. Phys. Chem. B **97**, 7277 (1993)

13 J. M. Coronado, A. J. Maira, J. C. Conesa, K. L. Yeung, V. Augugliaro, J. Soria, Langmuir **17**, 5368 (2001)

14 T. Berger, M. Sterrer, O. Diwald, E. Knozinger, J. Phys. Chem. B **109**, 6061 (2005)

15 M. Chiesa, M. C. Paganini, S. Livraghi, E. Giamello, Phys. Chem. Chem. Phys. **15**, 9435 (2013)

16 J. Chen, L.-B. Lin, F.-Q. Jing, J. Phys. Chem. Solids **62**, 1257 (2001)

17 C. Di Valentin, G. Pacchioni, A. Selloni, J. Phys. Chem. C **113**, 20543 (2009)

18 S. Livraghi, M. Chiesa, M.C. Paganini, E. Giamello, J. Phys. Chem. C **115**, 25413 (2011)

19 S. Livraghi, M. Rolando, S. Maurelli, M. Chiesa, M.C. Paganini and E. Giamello, J. Phys. Chem. C **118**, 22141 (2014)

20 D.C. Hurum, A.G. Agrios, K.A. Gray, T. Rajh M.C. Thurnauer, J. Phys. Chem. B **107**, 4545 (2003)

21 Y. Kohno, T. Tanaka, T. Funabiki, S.Yoshida, Phys. Chem. Chem. Phys. **2**, 2635 (2000)

22 C. Gionco, M.C. Paganini, E. Giamello, R. Burgess, C. Di Valentin, G. Pacchioni, J. Phys. Chem. Lett. **5**, 447 (2014)

23 C. Gionco, M.C. Paganini, E. Giamello, O. Sacco, V. Vaiano, D. Sannino, J. Energy Chem. **26**, 270 (2017)

24 C.Gionco, M.C. Paganini, E. Giamello, R. Burgess, C. Di Valentin and G. Pacchioni, Chem. Mater. **25**, 2243 (2013)

25 V.Polliotto, E. Albanese, S. Livraghi, P. Indyka, Z. Sojka, G. Pacchioni and E. Giamello, J. Phys. Chem. C **121**, 5487 (2017)

26 F. Morazzoni, R. Scotti, S. Volontè, J. Chem. Soc. Faraday Trans. **86**, 1587 (1990)

27 E. Cerrato, C. Gionco, M.C. Paganini, E. Giamello, J. Phys.: Condens. Matter **29**, 1 (2017)

28 L.E. Halliburton, N.C. Giles, N.Y. Garces, M. Luo, C. Xu, L.B.A. Boatner, Appl. Phys. Lett. **87**, 172108 (2005).

29 J.R. Brailsford, J.R. Morton, J. Chem. Phys. **51**, 4794 (1969)

30 G. Pinarello, C. Pisani, A. D'Ercole, M. Chiesa, M.C. Paganini, E. Giamello, O. Diwald, Surf. Sci. **494**, 95 (2001)

31 E.G. Panarelli, S. Livraghi, S. Maurelli, V. Polliotto, M. Chiesa and E. Giamello, J. Photochem. Photobiol., A **322**, 27 **(**2016)

32 C. P. Kumar, N.O. Gopal, T.C. Wang, M.S. Wong and S.C. Ke, J. Phys. Chem. B **110**, 5223 (2006)

33 A.V. Emeline, A.V. Panasuk, N. Sheremetyeva and N. Serpone, J. Phys. Chem. B **109,** 2785 (2005)

34 A.M. Volodin, S.E. Malykhin, G.M. Zhidomirov, Kinetics and Catalysis **52**, 605 (2011)

[35] N.B. Wong, Y.B. Taarit, J.H. Lunsford, J. Chem. Phys. **60**, 2148 (1974)

[36] C. Gionco, S. Livraghi, S. Maurelli, E. Giamello, S. Tosoni, C. Di Valentin, G. Pacchioni, Chem. Mater. **27**, 3936 (2015)

[37] S. Livraghi, F. Olivero, M.C. Paganini, E. Giamello, J. Phys. Chem. C **114**, 18553 (2010)

[38] M. Anpo, M. Che, B. Fubini, E. Garrone, E. Giamello and M.C. Paganini, Top. Catal. **8**, 189 (1999)

[39] T. Berger, O. Diwald, E. Knozinger, F. Napoli, M. Chiesa and E. Giamello, Chem. Phys. **339**, 138 (2007)